**Hayden A. Burgoyne**
Mem. ASME
GALCIT,
California Institute of Technology,
1200 E. California Boulevard,
Pasadena, CA 91125
e-mail: hburgoyne@caltech.edu

**Chiara Daraio**[1]
Mem. ASME
ETH Zurich,
Tannenstrasse 3,
Zurich 8092, Switzerland
e-mail: daraio@ethz.ch

# Elastic–Plastic Wave Propagation in Uniform and Periodic Granular Chains

*We investigate the properties of high-amplitude stress waves propagating through chains of elastic–plastic particles using experiments and simulations. We model the system after impact using discrete element method (DEM) with strain-rate dependent contact interactions. Experiments are performed on a Hopkinson bar coupled with a laser vibrometer. The bar excites chains of 50 identical particles and dimer chains of two alternating materials. After investigating how the speed of the initial stress wave varies with particle properties and loading amplitude, we provide an upper bound for the leading pulse velocity that can be used to design materials with tailored wave propagation.*
[DOI: 10.1115/1.4030458]

## Introduction

In elastic granular materials, the Hertzian contact law describes how particles interact with one another and governs the unique dynamics [1,2]. One-dimensional (1D) chains of uniform spherical elastic particles have shown unique dynamic properties, such as wave speed tunability [1,3], pulse reflections [4,5], shock trapping [6–8], and wave branching [9,10], all of which are useful for impact protection applications. Additional dynamics has been investigated for 1D dimer chains of two alternating materials; local resonances and reflections have been shown to slow the transmission of energy and have been suggested as a method for enhancing shock protection [4–7,11–15]. For acoustic excitations, dimer chains have been used to create materials with tunable band gaps with proposed applications in vibration isolation and acoustic filters [16–22]. However, these effects, for uniform and dimer chains, were all demonstrated at significantly lower forces than useful for most impact applications because they relied on the materials remaining elastic throughout the impacts [23].

For particles of most materials, plasticity occurs at relatively low contact forces, due to the stress concentrations arising in the contact region between spheres. To move toward practical impact protection applications, the dynamic response of 1D granular chains including the effects of plasticity has been recently investigated [24–27]. In order to design granular materials for impact mitigation and blast protection, it is necessary to understand how plasticity at the contacts changes the dispersion and energy dissipation of stress waves through these materials, and how these effects are controlled by constituent material properties and particle arrangements.

Differently than in the elastic Hertzian case, attempts to analytically describe the compression of elastic–plastic spheres have not been suitable for every materials and for many impact regimes [28]. However, the dynamic interaction between elastic–plastic particles has been described with numerical and experimental approaches [29–34]. In recent studies, simulations showed that the leading plastic wave propagating through elastic–plastic granular chains traveled slower than subsequent unloading and reloading waves due to residual plastic deformations changing the geometry of the contacts [24,27]. In these events, the unloading and reloading waves following the first compressive front operate in the elastic regime and exhibit the same properties as waves in elastic Hertzian granular chains. However, the initial plastic wave exhibits a different dynamic response governed by its unique nonlinear piecewise contact law. Previous work described the energy dissipation of a short impulse inducing plasticity in the initial particles of a long chain and the dependence of the wave speed on the excitation amplitude [24], but the dependence of the wave speed on the particles' material properties has not yet been investigated.

This work focuses on the properties of the leading wave, traveling through uniform and periodic granular chains consisting of alternating particle types, in response to a long duration impact. In such a loading scenario, plasticity continues to dissipate energy at each contact, significantly affecting the dynamics of wave propagation. We also investigate the effect of plasticity on wave propagation through dimer chains of alternating materials. Recent experiments have suggested that dimer chains of elastic–plastic spheres do not exhibit the same local resonances as elastic dimer chain [34]. It was observed that the amount of energy transmitted did not depend on the mass ratio of the particles and was dominated by plasticity effects instead of local resonances.

We simulate the response of these systems using a DEM, which includes a strain-rate dependent model for the dynamic contact interaction of elastic–plastic spheres [31]. We determine how the properties of the initial wave in the elastic–plastic granular chains compare to those in Hertzian chains and in chains described by a simplified linear contact law. We validate the model experimentally using a Hopkinson pressure bar coupled with a laser vibrometer. From the experimentally validated simulation results, we extract a model that relates the particles material properties to the leading wave velocity. In the dimer chains, we show the effect of local resonances on the energy transmission. We use the models to define design constraints for the creation of novel materials with engineered wave propagation properties.

## Numerical Approach

Numerical simulations of 1D chains of spheres were performed using a DEM code implemented in MATLAB [5]. Particles were treated as point masses that interact via an empirical contact law that models the force–displacement behavior of elastic-perfectly plastic spheres in dynamic compression using a piecewise, nonlinear formulation [31]. In selected cases, the results obtained with this dynamic contact law were compared to DEM simulations performed using Hertzian and linear contact laws. The contact forces on each particle were calculated at each time step and numerically integrated using a fourth-order Runge–Kutta method to get

particle displacements and velocities. It was assumed that the particles do not rotate or translate off-axis, reducing the dynamics to fully 1D interactions. Time step convergence studies were performed and a time step of $5 \times 10^{-8}$ s was used for all simulations. When the time steps were halved again, numerical values changed by no more than 0.01%.

The general form of the elastic–plastic contact used in simulation is given below in Eq. (1), and the full description of the model is provided in Appendix.

$$F(\delta) = \begin{cases} (4/3)E^* \sqrt{r^*}\delta^{3/2} & \text{for} \quad 0 < \delta < \delta_y \\ \delta(\alpha + \beta \ln \delta) & \text{for} \quad \delta_y < \delta < \delta_p \\ c_1 \sigma_y (2r^*\delta + c_2) & \text{for} \quad \delta > \delta_p \end{cases} \quad (1)$$

where $F$ is the contact force due to relative displacement, $\delta$, between spherical particles. $E^*$ and $r^*$ are functions of the Young's moduli and radii of the two spheres in contact. The empirical parameters $c_1$ and $c_2$ were obtained previously using finite element analysis (FEM) [31], and are also reported in the Appendix for convenience. The parameters $\alpha$ and $\beta$ were solved to ensure continuity of the force between regions. In order to capture strain-rate dependent plasticity, $\sigma_y$ was modified for rate-dependent materials using a Johnson–Cook type relation [31].

$$\sigma_y = \sigma_{y0}(1 - Cln(\dot{\varepsilon}/\dot{\varepsilon}_0)) \quad (2)$$

where $\sigma_{y0}$ is the yield stress measured at quasi-static strain rate $\dot{\varepsilon}_0$, and $C$ is the experimentally obtained Johnson–Cook parameter. The relative velocity between particles was used to define the strain rate: $\dot{\varepsilon} = |v_2 - v_1|/2R$, where $v_1$ and $v_2$ are the velocities of the two particles and $2R$ is the distance between centers of the two identical spheres of radius $R$. Previous FEM and experimental results have shown that this simplified definition of global strain-rate accurately captures the dynamics of the contact law despite sacrificing information regarding the local strain-rate of material within the spheres [31]. This model was formulated to describe the contact interaction between spheres of most metals and can capture the behavior of the contact between two dissimilar spheres as well. When dissimilar materials were used, it was assumed that all the plastic deformation occurs in the softer of the two materials and that only the plasticity properties of the softer material influence the contact properties [34,35]. Therefore, $\sigma_y$ was taken to be: $\sigma_y = \min(\sigma_{y1}, \sigma_{y2})$, the minimum of the yield stress of either of the two constituent materials. The rate dependence properties were selected to be the same as those of the softer material as well. One of the most important features of the elastic–plastic contact is the fact that the stiffness of the contact (i.e., the slope of the force–displacement law) transitions from amplitude dependent in the first and second regions to constant in the linear third region. The force at which this transition occurs, $F_P$, is fully defined in the model as a function of the material properties of the contacting spheres and is given in Appendix.

Unloading was assumed to be purely elastic, with the formulation given in Appendix [30]. After unloading, subsequent reloading of the contacts follows the Hertzian unloading curve back up until the previous maximum contact force has been reached and plastic deformation begin again. The history of plastic deformation at each contact point was therefore stored in a global variable and used to determine whether the current loading was elastic or plastic. The force–displacement law of the elastic–plastic contact is shown in Fig. 1(a) as the blue curve. The transitions between piecewise regions are shown as dotted vertical lines.

Without plasticity, the contact between metallic spheres is captured by the Hertzian contact law,

$$F_H(\delta) = (4/3)E^* \sqrt{r^*}\delta^{3/2} = K_H \delta^{3/2} \quad (3)$$

where we define $K_H$ as the Hertzian stiffness. The Hertzian contact law is equivalent to the initial region of the elastic–plastic contact before plasticity initiates. The Hertzian contact law is shown in Fig. 1(a) as the green curve.

In order to isolate the contribution of the nonlinear region in the elastic–plastic contact law to the dynamics of the chain, we compared the full elastic–plastic contact model with a contact model that includes only the linear contribution of the plastic region,

$$F_L(\delta) = c_1 \sigma_y (2r^*\delta) = K_L \delta \quad (4)$$

where we define $K_L$ as the linear stiffness. The stiffness of this linear model is the same as the elastic–plastic model given in Eq. (1) when $\delta > \delta_p$. For the linear contact-law, the same formulation for unloading was used as in the elastic–plastic model given in Appendix. The linear contact-law is shown in Fig. 1(a) as the red curve.

In DEM simulations of 1D chains of spheres, the initial conditions selected specified either the velocity or the force profile of the first sphere in the chain. When simulating Hopkinson bar experimental tests, we used as initial conditions the velocity profiles measured experimentally at the end of the incident bar. In all other simulations, a square velocity or force pulse was applied to the first sphere. After this initial pulse was applied, the particle could move freely like the other particles in the simulations. The final sphere was assumed to be in contact with a 1D linear medium having the same properties as the transmission bar used in experiments (i.e., wave speed, density, and area). When processing the numerical results, we calculated the local wave speeds by taking the difference in the arrival times of the stress wave at each subsequent particle and dividing it by the distance between those particles. The arrival time for each particle was defined as the time for which the particle reached 1% of the initial velocity of the first particle, or 1% of the maximum velocity of the first particle.

## Experimental Setup

A Hopkinson pressure bar was used to impact chains of metallic spheres. A schematic of the experimental setup is shown in Fig. 1(b). Strain gauges on the incident and transmission bars measured the incident, reflected, and transmitted stress waves. The spheres were held between the bars and confined to move only along the axis of the chain by a 3D printed plastic tube. A truncated (3/4) sphere was used as the first particle in flat contact with the end of the incident bar. This ensured that the first particle had the same velocity profile as the end of the incident bar, as measured by the strain gauges, and that all energy was dissipated in the contacts between spheres. The flat side of the first particle remained in contact with the incident bar through the duration of the data acquisition. A copper pulse shaper was used between the striker and incident bar to ensure repeatable impacts for all experiments. The velocity profile at the end of the Hopkinson bar is given as a function of the strains measured by the incident strain gauge during the incident and reflected pulses,

$$v_{bar}(t) = c_i(-\varepsilon_i(t) + \varepsilon_r(t)) \quad (5)$$

where $c_i$ is the elastic wave speed in the Hopkinson bar and $\varepsilon_i$ and $\varepsilon_r$ are the strains during the incident and reflected pulses. The incident strain is translated forward in time by $c_1$ times the distance from the gauge to the end of the bar, while the reflected strain is translated backwards in time by the same amount such that they are summed when both are at the end of the bar. A dispersion correction was applied to the incident and reflected waves as in Ref. [36] in order to account for dispersion in the 1D bar, yielding smoother applied velocity profiles.

The spherical particles used in experiments had a diameter of 6.35 mm and were made of stainless steel 440 c, stainless steel 302, aluminum 2017, and brass 260, purchased from McMaster-Carr. Truncated (3/4) spheres of the same materials were
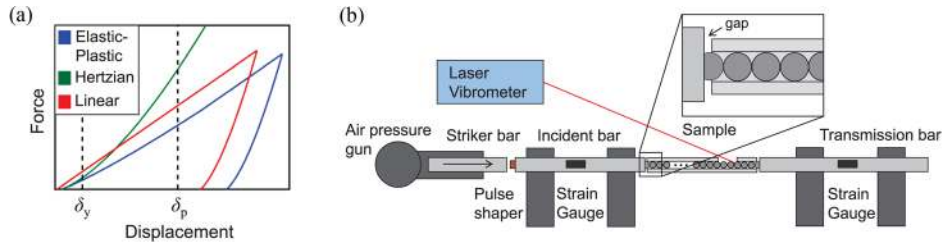
**Fig. 1** (*a*) Schematics of the three force–displacement relations used in the numerical simulations: elastic–plastic (blue, right-most curve), Hertzian, elastic (green, left-most curve), and linear (red, centered curve). Dotted vertical lines show transitions between regions in the elastic–plastic model with $\delta_y$ representing the displacement at which plasticity initiates and $\delta_p$ representing the displacement at which the linear regime begins. (*b*) Schematic diagram of the experimental setup showing the Hopkinson pressure bar with the laser vibrometer. The samples consisted of chains of 50 spheres, 6.35 mm in diameter, enclosed in a 3D printed tube with a window for the laser to measure the particle velocity of the 40th sphere.

purchased from BalTec. In simulations, the particles' material properties were selected from the ranges given by the manufacturer to match simulations of single contacts (Table 1) [31]. Sample holders were 3D printed with an Objet500 Connex printer using a rigid plastic, VeroBlack [37], and were designed to have an inner diameter the same as the spheres. The tubes ensured that the chains of spheres remained aligned along the axis of the Hopkinson bar without rattling, but did not create appreciable friction. The 3D printed inner surface was thoroughly cleaned after printing and spheres could slide freely within the tube without the need for lubrication. To avoid the transmission of stress waves through the holder, the length of the tube was made slightly shorter than the chain of spheres, forming a small gap between the holder and the bars (see inset of Fig. 1(*b*)). Because the stress waves were not transmitted through the plastic holder, the holder was not included in the simulations. Vaseline was used to adhere the truncated spheres to the incident and transmission bars to ensure they were centered and aligned. The tube containing the remaining 48 spheres was then placed between the two aligned truncated spheres. The rigid plastic tube was stiff enough, but light enough that it could support its own weight without sagging while held firmly between the incident and transmission bars ensuring no gaps between spheres.

We used strain gauges on the incident and transmission bars to detect the incoming, reflected and transmitted waves after interaction with the granular chains. In addition, a Polytech laser vibrometer was used to measure the velocity profile of one of the spheres in the chain. This direct measurement of the dynamics of particles inside the sample allowed testing longer chains and enabled a more direct comparison of the experimental results with numerical simulations. The laser vibrometer data and strain gauge data were both supplied to a data acquisition computer such that they were triggered together, ensuring that the time recorded by all sensors were synchronized. We tested chains of 50 spheres, consisting of identical particles (i.e., uniform chains) and periodic arrangements of particles alternating two different materials (i.e., dimer chains). In all configurations studied, the length of the chains was such that the forces transmitted through the chains were significantly reduced, and the signal measured by the strain gauges in the transmission bar was indistinguishable from the experimental noise.

**Table 1 Material properties used for simulations [31]**

| Material | Density (units) | Young's modulus (units) | Yield strength (units) |
|---|---|---|---|
| Stainless steel 440 | 7650 | 200 | 1896 |
| Stainless steel 302 | 7860 | 200 | 600 |
| Aluminum 2017 | 2700 | 75 | 400 |
| Brass 260 | 8530 | 110 | 670 |

The laser vibrometer was used to measure the particle velocity of the 40th sphere throughout the impact.

## Results and Discussion

**Properties of Waves in Chains of Elastic–Plastic Particles.** Prior studies of wave propagation in elastic–plastic 1D chains of spheres focused on the energy dissipation of short impulses and on the effects of impact amplitude and duration on the wave speed [24,25,27]. However, the experiments reported in these studies were limited to testing short chains, and can only characterize the transmitted waves after the impact. In this work, we study long chains of particles, and focus on the understanding of the dynamics of wave propagation while plasticity is occurring at the contacts, the most relevant regime for energy dissipations during an impact. Our approach also allows a more direct comparison of the experiments with numerical simulations.

To understand the effect of plasticity and nonlinearity on the wave propagation, we performed simulations of the dynamics of 1D chains of 50 particles with elastic–plastic, Hertzian, and linear models describing their contacts (Fig. 2). In these simulations, we applied a 20 m/s step change in initial velocity to the first particle in the chain, and observed the wave front as it propagated through the materials. The dynamic response of both Hertzian and harmonic linear chains to such initial conditions is well known. Hertzian chains support the formation and propagation of a steady front that, after some initial transient effects, propagates through the chains without changing shape due to dispersion [1,12]. The evolution of the wave front shape is shown in Fig. 2(*a*) for a Hertzian material. In this figure, the different curves represent the velocities of all particles, superimposed and translated based on the arrival time of the wave. The arrival time of the wave front at each particle was defined as the time at which the particle reached 1% of the applied initial velocity (0.2 m/s). Although the speed of nonlinear waves in Hertzian chains is frequency independent, it is amplitude dependent. The leading wave speed, $V_H$, is given by [38]

$$V_H = 0.68 \left( \frac{E^*}{r^* \rho^{3/2}} \right)^{1/3} F_M^{1/6} \qquad (6)$$

where $\rho$ is the density of the constituent material and $F_M$ is the maximum contact force. The velocity can also be rewritten to show the dependence of the wave speed on the Hertzian stiffness as defined in Eq. (3) as [38]

$$V_H = 0.87 \frac{K_H^{1/3}}{\sqrt{r^*} \rho} F_M^{1/6} \qquad (7)$$

In harmonic lattices with linear force–displacement relations, the dispersion relation describes the speeds at which the various
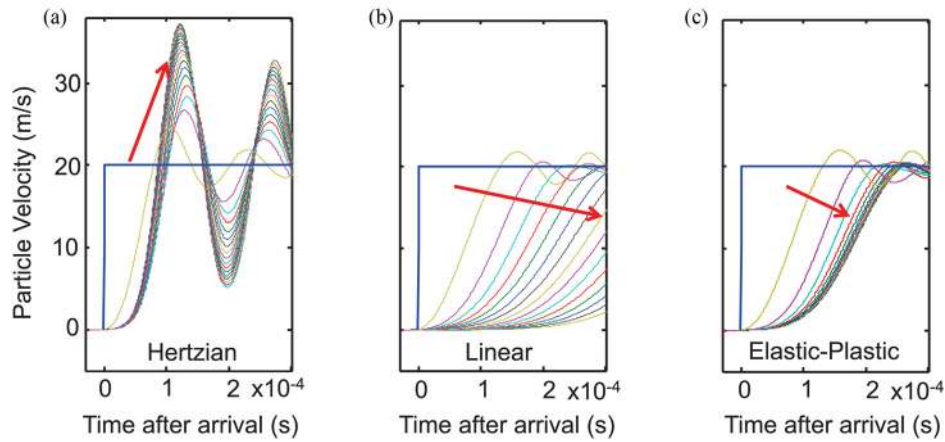
**Fig. 2** Numerical simulations comparing the dynamic response of chains of 50 particles, subjected to a 20 m/s constant velocity, governed by different contact dynamics. The different color curves represent all particle velocities after the arrival of the initial wave front. The velocities curves were translated based on the arrival time of the wave on each particle. (*a*) Response of a Hertzian chain; (*b*) response of a harmonic chain of linear springs; and (*c*) response of a chain of elastic–plastic particles. Arrows indicate the movement of the velocity wave front at progressively later positions in the chain. The arrow points toward the steady wave front that is formed in (*a*) and (*c*) in the Hertzian and elastic–plastic cases, respectively, while in linear case the wave front continues to spread in the direction of the arrow due to dispersion.

frequency components of the initial disturbance move through the chain [39–41]. Because the different frequency components move at different velocities, a steady front is not formed in linear materials and the pulse widens as it travels down the chain. The evolution of the wave front shape for a chain of masses with linear contact interactions is shown in Fig. 2(*b*). Again in this figure the particle velocities of each particle were superimposed and translated based on the arrival time of the wave as defined previously. The frequency content separates due to dispersion and the peak of the wave appears to arrive at progressively later times after the initial arrival as the wave spreads. While the speeds of linear waves are dependent on the frequency content, there is no direct dependence on the amplitude of the initial excitation because the stiffness of the contact is constant for all amplitudes. The phase velocity of frequency component is $V_{\mathrm{L}} = \omega/k$, where $\omega$ and $k$ are the frequency and wave number, respectively, of the normal modes of the linear lattice. $\omega$ and $k$ are related by the dispersion relation [39].

$$\omega(k) = 2\sqrt{\frac{K_{\mathrm{L}}}{M}}|\sin kR| = \sqrt{\frac{3K_{\mathrm{L}}}{\pi R^3 \rho_{\mathrm{avg}}}}|\sin kr| \qquad (8)$$

where $M$ is the average mass of the particles, $R$ is the average radius of the spheres, and $\rho_{\mathrm{avg}}$ is the average density of the constituent materials. The maximum phase velocity for any frequency component, $V_{\mathrm{L,max}}$, occurs for long wave length excitations in the limit as $k$ goes to 0 and is given by

$$V_{\mathrm{L,max}} = \sqrt{\frac{3K_{\mathrm{L}}}{\pi R \rho_{\mathrm{avg}}}} \qquad (9)$$

In elastic–plastic chains the dynamics are different. When the initial impact is large enough to induce plasticity at the contacts, the particle's loading begins in the nonlinear region described by the Hertzian contact, while the maximum force occurs in the linear regime. The shape of the wave front after a velocity pulse in the elastic–plastic case exhibits unique features compared to waves in the other two types of materials. The evolution of the

wave front shape is shown in Fig. 2(*c*). After an initial transient region (∼5 particles long), in which dispersion seems to occur, a steady wave front forms and continues to propagate unperturbed.

Plasticity has a major effect on the wave's propagation in 1D granular systems. Defining a realistic elastic–plastic contact model is essential to capture the correct dynamic behavior of such systems. Both the nonlinear and linear regimes play essential roles in the unique dynamics of these granular systems. The initial contact nonlinearity, before the onset of plasticity, plays an important role in determining the chain's dispersion behavior, and controlling the frequency and amplitude dependence of the leading wave velocities, while the linear regime determines the apparent stiffness of the chain during plastic deformation.

We performed parametric studies using DEM to determine how, in elastic–plastic chains, the leading wave speed depends on the material properties of the constituent particles. We compared the results with similar ones obtained for Hertzian and linear chains. First, the density of the constituent particles was varied while the Young's modulus and yield stress of the material were kept constant. We excited the 50-particle chains with an impulse of $100 \times 10^{-6}$ s with constant force amplitude of twice the force required to reach the linear plastic regime in the elastic–plastic contact law ($2F_{\mathrm{P}}$). In all simulations, the chains consisted of particles with a Young's modulus of 100 GPa and a yield stress of 500 MPa, while the density was varied in ten steps from 1000 kg/m$^3$ to 15,000 kg/m$^3$. For each chain, local wave velocities of each particle were calculated and then averaged over all particles between the 10th and the 40th particle. The results are shown in Fig. 3(*a*). Fitting curves (solid lines in Fig. 3(*a*) show that all three contact models share an inverse square root dependence on the density of the constituent material.

Next, we performed parametric studies using DEM to obtain the leading wave velocity's dependence on the stiffness of the contact. The yield stress of the constituent particles was varied while the Young's modulus and density of the material were kept constant. As before, an impulse of $100 \times 10^{-6}$ s with amplitude of $2F_{\mathrm{P}}$ was applied to 50-particle chains of each material for all three contact laws. A Young's modulus of 100 GPa and a density of 5000 kg/m$^3$ was used for all simulations, while the yield stress was varied in ten steps from 100 MPa to 2500 MPa. For each

material, local wave velocities of each particle were calculated and then averaged over all particles between the 10th and the 40th particles. The results are shown in Fig. 3(*b*). Fitting curves (solid lines in Fig. 3(*b*)) show that the Hertzian material has a cube root dependence on the stiffness as predicted in Eq. (7), while both the linear and elastic–plastic materials exhibit the square root dependence predicted in Eq. (8). Therefore, we see that the leading wave speed of elastic–plastic chains scales in the same fashion as the simplified linear-chains.

In the plastic region, the stiffness of the contact is not amplitude dependent, however in elastic–plastic chains the wave speed is amplitude dependent. This is due to the fact that before reaching the plastic zone, the contact force rises through the Hertzian region, which is amplitude dependent. To investigate the effect of the excitation amplitude on the wave speed in elastic–plastic chains in comparison with Hertzian and linear chains, we calculated the response of the different contact laws after the application of impulses with greatly varying amplitude. Impulses with duration $100 \times 10^{-6}$ s and amplitudes ranging from 10 N to 10 kN were simulated on chains of 50 particles. The particles' material properties were kept constant with a Young's modulus of 100 GPa, yield stress 500 MPa, and density 5000 kg/m$^3$ ($F_P$ = 584 N). The simulated leading wave speeds are shown versus the logarithm of the applied force, normalized by $F_p$, as the blue and green markers in Fig. 3(*c*) for elastic–plastic and Hertzian granular chains, respectively. The green curve in Fig. 3(*c*) shows the dependence of the wave speed in the Hertzian material on $F^{1/6}$ as predicted in Eq. (7). The red line in Fig. 3(*c*) shows predictions for the maximum velocity component of the harmonic linear material given in Eq. (9). As the force increases, the elastic and elastic–plastic wave speeds diverge. Once the amplitude of the force reaches $F_p$, the leading wave speed of the elastic–plastic material begins to asymptotically approach the prediction of the fastest component of a harmonic lattice with the same stiffness as the elastic–plastic linear regime. Therefore, Eq. (9) represents a bound of the leading wave speed in the elastic–plastic 1D material, although the required force to reach this bound is highly material dependent. Figure 3(*c*) shows that for large amplitude impacts (inducing forces greater than the force required to reach the plastic regime, $F_p$) the leading wave velocity changes by only 10% over an order of magnitude change in the force. For impacts in which the plastic regime is reached, 1D elastic–plastic chains exhibit unique dynamics where the leading wave velocity has no frequency dependence, relatively little amplitude dependence, and is almost solely a function of the material properties of the constituent particle. Combining the velocity bound in Eq. (9) with the elastic–plastic contact law presented by Burgoyne and Daraio [31] it is possible to derive a model to predict the maximum wave speed ($V_{max}$) in 1D granular materials when plastic deformation is occurring. $V_{max}$ can be expressed in terms of the material properties of the constituent particles for high amplitude impulses as

$$V_{max} = \sqrt{\frac{3K_L}{\pi R \rho_{avg}}}$$

$$K_L = 2\pi r^* \sigma_y \left[ -6.76 \left( \frac{E^*}{\sigma_y} \right)^{-0.14} + 6.30 \right] \quad (10)$$

**Experimental Validation and Simulations.** Hopkinson bar experiments were performed in order to verify that DEM simulations captured the leading wave velocity and energy dissipation properties of long 1D chains of spheres. The raw forces in the incident and transmission bars as measured with the strain gauges are shown in Fig. 4 for uniform chains of 25 and 50 stainless steel 440 c spheres. The incident and reflected force pulses were nearly identical between each experiment comprised of stainless steel 440 c spheres. Stainless steel 440 c had the highest yield stress of any of the materials used and therefore transmitted the most force through the chain. The transmitted force through the shorter, 25 particle chains demonstrated the repeatability between experiments.
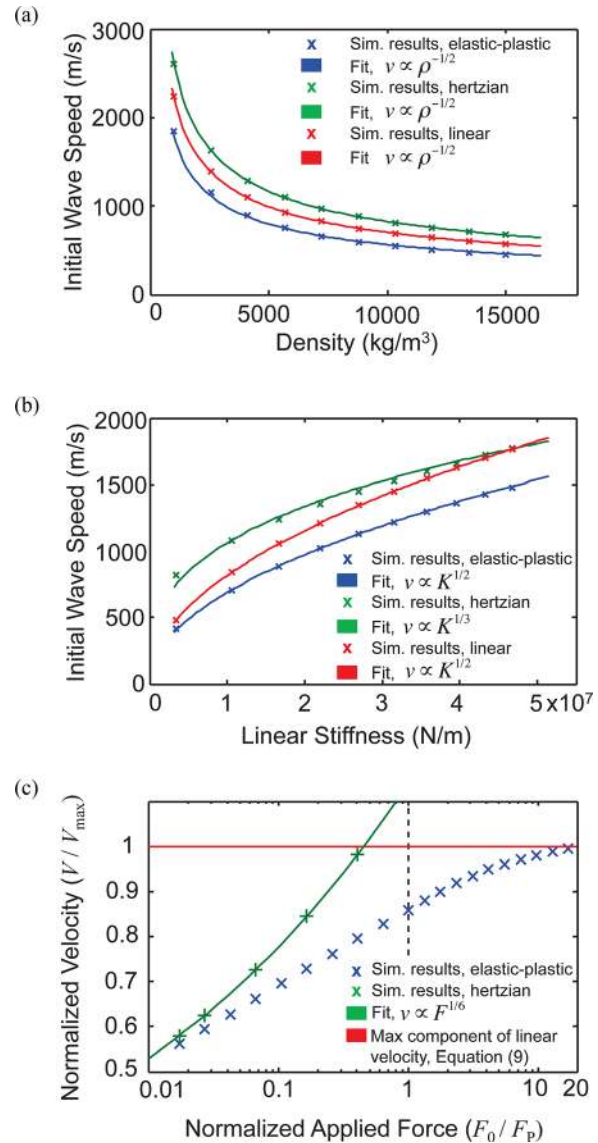


**Fig. 3** Numerical results of parametric studies of the propagating wave speed as a function of (*a*) the density and (*b*) stiffness of the particles material. The plots compare the results obtained for chains with elastic–plastic contacts (blue, bottom-most curves), Hertzian contacts (green, top-most curves), and linear contacts (red, centered curves), subjected to a 2$F_p$ impulse. (*a*) Markers represent the average wave speed observed in each DEM simulation with solid lines showing the wave speed dependence on the square root of the inverse of density. (*b*) Markers represent the average wave speed observed in each DEM simulation with solid lines showing the wave speed dependence on either the square root or the cube root of the stiffness. (*c*) Numerical results showing the dependence of the normalized wave velocity on the normalized applied force, plotted on a logarithmic scale. Markers represent the average wave speed observed in each DEM simulation, with "×" representing elastic-plastic and "+" representing Hertzian. The green, left-most curve shows the dependence of the wave speed in the Hertzian material on $F^{1/6}$. The red, horizontal line is the maximum velocity component of a harmonic chain given by Eq. (9). The black, vertical, dashed line shows $F_p$, the force at which the linear regime begins in the elastic–plastic material and the local wave speed begins to asymptotically approach the bound, as the amplitude increases.

However, for 50 spheres, the transmitted force was attenuated to the point where noise in the strain gauges becomes very significant, as seen in the green curve in Fig. 4. The forces were even more
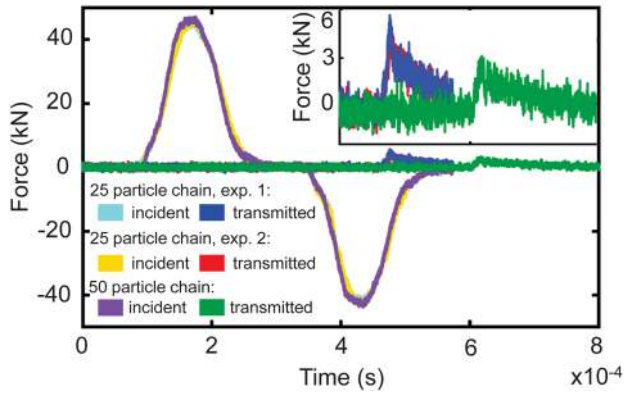
**Fig. 4 Experimentally measured forces within the incident and transmission bars of the Hopkinson bar setup as measured by the strain gauges for 25 and 50 particle chains of uniform stainless steel 440 c spheres. For the two experiments with 25 particles chains, the cyan and yellow curves (overlapping larger pulses) show the forces in the incident bar while the blue and red curves (overlapping small pulses also shown in inset) show the forces in the transmission bar. For the experiment with a 50 particle chain, the magenta curve (overlapping large pulse) shows the forces in the incident bar while the green curve (small pulse also shown in inset) shows the forces in the transmission bar. The inset shows the transmitted forces for the three experiments zoomed in to show repeatability between experiments as well as the influence of experimental noise.**

greatly attenuated in chains of other materials, and therefore the use of the laser vibrometer was necessary to measure particle velocity late in the long chains of particles.

Uniform chains of 50 aluminum and stainless steel 302 particles, as well as dimer chains of alternating particles, were impacted using the Hopkinson bar and measured with a laser vibrometer. The velocity profile reaching the end of the incident bar, in contact with the first sphere, was calculated from the incident and reflected waves measured by the strain gauge on the incident bar using Eq. (5). The experimental velocity profiles are shown as the blue curves in Figs. 5(a)–5(c). The velocity profile of the 40th particle was measured by the laser vibrometer and is shown for each experiment as the red curves in Figs. 5(a)–5(c).

We simulated the experimental response of these chains applying the experimental, incident velocity profiles to the first sphere in the chain. The simulated velocities of the 10th, 20th, 30th, and 40th spheres are shown as the yellow, magenta, cyan, and green curves, respectively, in Figs. 5(a)–5(c). The DEM simulations predict the particle velocity profile of the 40th particle extremely well, capturing correctly the magnitude of the particle's velocity, the arrival time of the leading plastic wave, the arrival of the reflected wave off the end of the sample and the local oscillations of particle. The importance of including strain-rate dependence in materials like stainless steel 302 is evident in Fig. 5(b). When the quasi-static yield stress is used in the model without utilizing the Johnson–Cook type rate dependence, the velocity profile of the 40th sphere is not predicted correctly by the simulations, as shown by the dashed gray line in Fig. 5(b). For rate-dependent simulations of steel 302, a Johnson–Cook parameter of 0.025 was used [31].

Figure 5(d) shows the simulated force at the first contact versus simulations of the force felt by the 50th (final) sphere, after the velocity profile of the incident bar as measured by the strain gauges during the experiment was applied to the first sphere. While the incident velocity profile was nearly identical between experiments, the applied force was material dependent and varied between experiments due to the differences in stiffness of the contacts between particles and masses of the particles. The maximum force after traveling through chains of 50 spheres was reduced by 49.6% in the stainless steel 302, 39.7% in the aluminum, and 57.0% in the alternating dimer chain. The forces on the final bead in the dimer chains, as shown by the red curve in Fig. 5(d), are

spread over a longer time period and have a smaller transmitted maximum force. In many impact protection applications, the ratio of the input force to the maximum transmitted force is the most crucial measure of protection.

In order to gain further insights into the details of the dynamics observed in the experiments of these materials, we simulated a $100 \times 10^{-6}$ s impulse of amplitude $2F_p$ on 50-particle chains of steel 302, aluminum, and an alternating dimer chain. X-T diagrams showing particle position over time are shown in Fig. 6, with colors scale depicting the magnitude of the contact force between each particle, normalized by the applied force. For each material we observe the initial pulse traveling at a nearly constant speed determined by the stiffness in the linear regime for that material. Once the initial force is removed after $100 \times 10^{-6}$ s, the unloading wave travels through the chain at a faster speed, governed by the elastic unloading of the particles, followed by subsequent reloading waves as the particles continue to collide within the chain. The dynamics of the nonuniform chain (Fig. 6(c)) are visibly different than the behavior of the single material chains. Heterogeneous chains of Hertzian materials have been shown to have wave speed dependence on the mass ratio of the constituent spheres, whereas wave speeds in the harmonic linear chains only depend on the average density of the constituents [11–13,39–41]. For chains of spheres with identical radii but two alternating materials, the leading wave velocity in the dimer elastic–plastic materials shown in Fig. 6(c) does not show any dependence on the mass ratio, only the average of the densities of the two materials (also shown experimentally [34]). After the arrival of initial plastic wave, trailing waves operate within the elastic regime, and internal reflections associated with local resonances are visible in the XT diagram of the dimer chain (Fig. 6(c)), behind the leading plastic wave. These elastic internal reflections depend on the particles mass ratio and slow the transfer of energy to the leading plastic front [11–13]. Therefore, the two types of waves in these materials exhibit inherently different behaviors: the leading wave which causes plasticity does not excite local resonances and its speed depends only on the average mass, while the trailing elastic waves do excite local resonances and cause internal reflections. In dimer chains, this results in more collisions, sustained for longer times, after the initial impact has passed. The forces transmitted at the end of the chain are spread over a longer time period and more uniformly (confirming the experimental velocity measurements in Fig. 5(c) and simulation of transmitted force in Fig. 5(d)). Other periodic composite materials for impact applications have also demonstrated wave propagation properties that exceed those of either constituent component. For example, the shock speed through layered polycarbonate/stainless steel 304 and polycarbonate/ aluminium was also shown to be significantly slower than shocks in the constituent materials also due to internal reflections [42].

We performed additional Hopkinson bar experiments with uniform and dimer chains of brass and stainless steel 440 particles (see properties in Table 1) and compared the results with DEM simulations (Fig. 7). As shown for aluminum and steel 302 chains previously, the numerical results agreed well with the experimental data. The markers in Fig. 7(a) show the arrival speed measured experimentally on the 40th sphere in all chains. The arrival speed is defined for each sphere as the total distance of the center of the sphere from the end of the incident bar divided by the time at which the particle velocity reaches 1% of the applied velocity (typically 0.12 m/s for these experiments). The arrival speed of the wave to a point in the chain is therefore the average of the local wave speed between each particle before that point. This measure was used instead of the local wave speed used in Fig. 3 because the laser vibrometer measured the cumulative arrival time to the 40th sphere and not the subsequent arrival time between adjacent spheres. We compared the experimentally measured arrival speeds at the 40th particles to the predicted arrival speeds throughout the chain for each of the experiments. Solid lines in Fig. 7(a) represent uniform materials while dashed lines represent the different dimer combinations. The simulations capture the
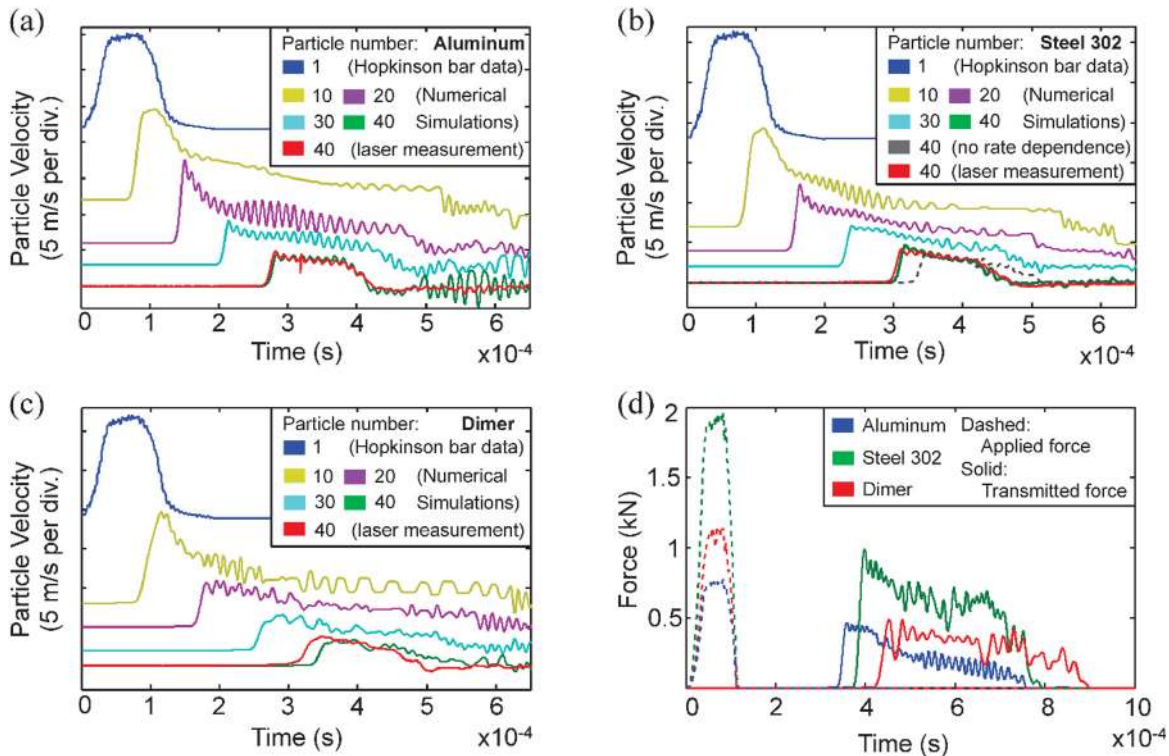
**Fig. 5** Experimental results obtained with the Hopkinson bar setup compared with corresponding numerical simulations for (*a*) uniform chains of aluminum particles, (*b*) uniform chains of stainless steel 302 particles, and (*c*) dimer chains. The blue and red (top-most and bottom-most) curves represent experimentally measured velocities for the first (blue, top) and the 40th (red, bottom) spheres. The yellow, magenta, cyan, and green (progressively lower) curves represent numerical simulation for the 10th, 20th, 30th, and 40th particles in the chains. The dashed dark-gray line in (*b*) shows the numerical results obtained when strain-rate dependence is ignored and the yield stress is assumed to be the same as the quasi-static yield stress of stainless steel 302. (*d*) Plot of the simulated contact force between the first and second particles after the experimentally measured velocity profile is applied, and the simulated force profile of the final bead in 50 sphere chains of aluminum particles (blue, bottom-most), stainless steel 302 particles (green, top-most), and an alternating dimer (red, centered).

leading wave speed and particle velocity amplitude for a wide range of different types of metallic spheres and for dimer chains of alternating material. For the uniform chains, the average error between the measured and simulated arrival velocities was 1.15%,

likely due to variability in the material properties of the spheres. For the dimer chains, simulated arrival times were all consistently underestimated by an average of 3.13%. This suggests that the contact between dissimilar materials is slightly stiffer than
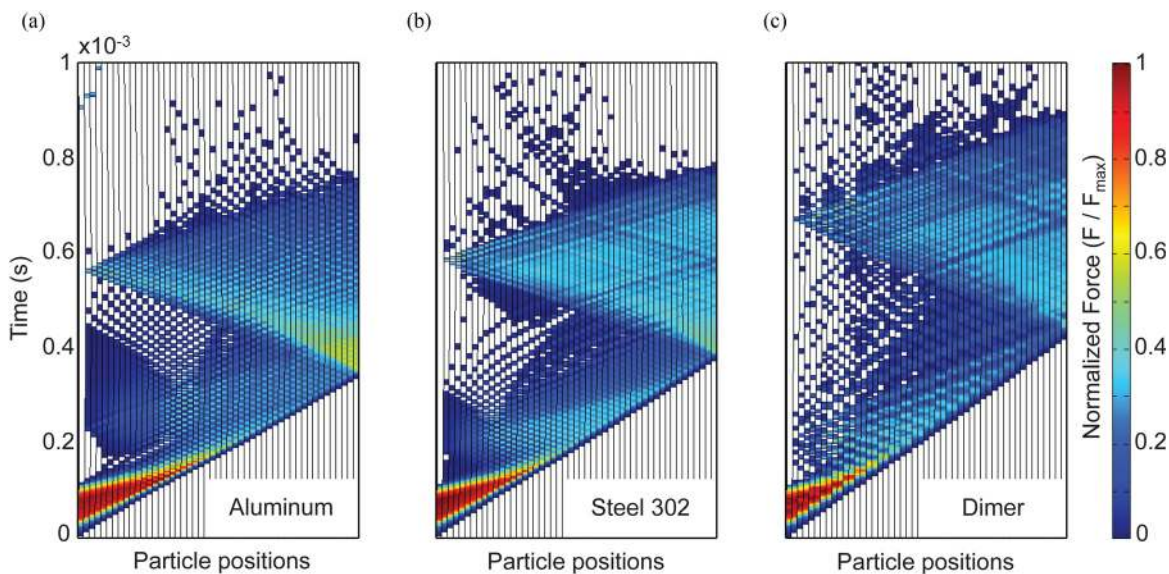


**Fig. 6** X-T diagrams showing the wave propagation in time through chains of 50 particles, assembled with particles of different materials. All chains were excited by a pulse of amplitude $2F_P$ and $100 \times 10^{-6}$ s duration. The color scale represents the contact forces between particles, normalized by the applied force. (*a*) Chain of aluminum particles, (*b*) chain of stainless steel 302 particles, and (*c*) dimer chain consisting of alternating stainless steel 302 and aluminum.

predicted, and this is most likely a consequence of the assumption in the model that stiffness in the linear regime is solely a function of the softer material's properties.

Figure 7(b) shows the leading wave velocities after a $2F_P$ impulse was applied to each of the material combinations shown in Fig. 7(a). The leading wave velocities are normalized as: $V_{\text{norm}} = V/V_{\text{max}}$, where $V_{\text{max}}$ is given by Eq. (10). The vertical dashed line represents the approximate location at which the contact forces drop below $F_P$ and stiffness becomes amplitude dependent once again. Before this line, when the contact forces are all in the plastic linear regime, the normalization causes all curves to overlap and we observe nearly no amplitude change. All curves converge to around 90% of the maximum possible wave speed because of the amplitude dependence demonstrated in Fig. 3(c). The alternating dimer combinations show significant variations in the arrival times between heavy versus soft constituents, but the average still falls on the normalized curve. As stated earlier for chains of particles of equal radius with alternating material properties, there is no dependence of the leading wave velocity on the mass ratio of the particles that comprise the dimer, only on their average density. Once the contact forces drop below the purely linear regime, the leading wave speed becomes more amplitude dependent, as seen in Fig. 3(c), and the curves diverge slightly and begin to slow as energy continues to be dissipated in the intermediate regime between the Hertzian and plastic zones in the elastic–plastic contact law.
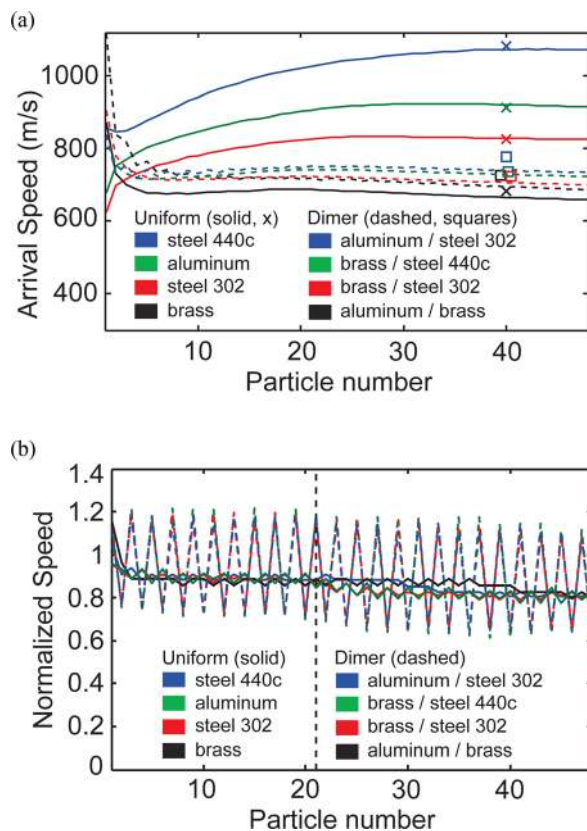


**Fig. 7** (*a*) Arrival speed of the wave front as it travel through chains of 50-particles of different materials (Table 1). Numerical results (lines) are compared with experiments (markers) for the particle's velocity measured by the laser vibrometer in the 40th particle. Solid lines represent the arrival speeds in uniform chains. Dashed lines show the same results for dimer chains. (*b*) Numerical results showing the local wave speed as it travel through the 50-particles chains, normalized by the wave speed bound given in Eq. (10).

**Designing Wave Properties.** We have shown that the leading plastic wave in elastic–plastic granular chains forms a steady propagating wave front, with a speed that is dependent on amplitude, but is independent of frequency content of the excitation and is bounded by the long-wavelength speed of a simplified linear model with the same stiffness. We have also shown that our model predicts correctly the leading wave properties for both uniform and dimer chains. These foundations provide the necessary insight to predict the behavior of new uniform materials, new combinations of dimer materials, and new rationally designed particles to obtain materials with unique wave propagation properties. Figure 8 shows a design surface, which relates the linear stiffness and the average density of constituent particles with the predicted bound of the leading wave speed given by Eq. (10). We can use this surface to design 1D materials for which the speed of plastic stress waves cannot exceed the predicted value. The real materials used in experiments, as well as others, like tungsten carbide, are shown by markers with blue stems. Brass has the lowest predicted wave speed with 833 m/s, while stainless steel 440c has the highest with 1347 m/s, a factor of 1.6 larger. Alternating dimers using the same materials are shown by markers with red stems. Chains consisting of a combination of aluminum and tungsten carbide particles have the lowest predicted wave speed, with 629 m/s, a factor of 2.14 lower than the uniform stainless steel 440c wave speed. By using alternating dimers, the design space of wave speeds has been expanded.

Additionally, the surface plot in Fig. 8 allows predicting the behavior of engineered particles. For example, we see that materials with the highest density and lowest stiffness lead to the slowest leading wave velocity. If we were to coat a tungsten carbide particle with aluminum, such that the final particle had the stiffness of aluminum but a density five times higher, Eq. (10) predicts that we would obtain a wave speed of 489 m/s. If we were to create a hollow particle of tungsten carbide such that the stiffness properties were not changed, but the final particle density was five times less, Eq. (10) predicts that we would obtain a wave speed of 3011 m/s. These two engineered materials are shown by the markers with black stems in Fig. 8. Such particles increase the design space such that we obtain a factor of 6.2 between the fastest and slowest materials. However, these hollow/coated particle chains would have to be used within a range of impacts that do not violate certain assumptions: first that the plastic region is small enough that it is not altered by the presence of another material in the core of the particle, and second that the wave speed is much slower than the time it takes for the stresses to travel from one end of the particle to the other. These assumptions are unlikely to be valid for very large amplitude impacts, but the design surface allows us to easily visualize how new combinations of materials or engineered particles are likely to dynamically behave.

## Summary and Future Work

We investigated the dynamics of high-amplitude stress waves propagating through 1D chains of spherical particles. In order to understand the effect of each regime of the piecewise nonlinear, elastic–plastic contact law, we compared chains of elastic–plastic spheres, with chains of purely elastic particles interacting via the Hertzian contact law, as well as with harmonic chains having the same linear stiffness as the one found in the linear regime of the elastic–plastic model. We reported that the elastic–plastic chains showed no dispersion even when forces reached the fully plastic linear regime. As in a chain of Hertzian particles, the frequency components of the wave all propagated at the same velocity, unlike in a typical linear material. However, by varying the density and contact stiffness of the constituent particles, we found that while plasticity is occurring at the contacts, the speed of the leading wave in the elastic–plastic chain scales with the material properties in the same manner as wave velocities in a harmonic chain of particles with linear contacts. We showed that the
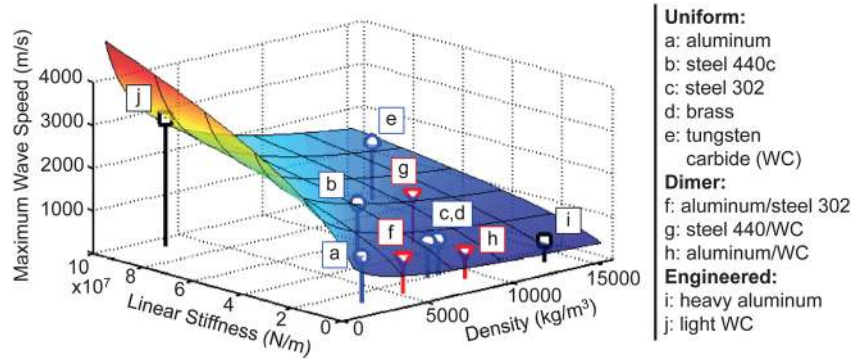
**Fig. 8** Surface plot relating the maximum wave front speed as a function of the linear stiffness of the contact and the average density of the constituent particles, calculated using Eq. (10). Markers and stems show locations of uniform chains of particles with materials listed in Table 1 (blue, circle markers), alternating dimers of those materials (red, triangle markers), and engineered particles such as heavy core aluminum and hollow tungsten carbide (black, square markers).

harmonic prediction of velocity of the frequency component with highest speed represented an amplitude-dependent bound on the maximum possible velocity in the elastic–plastic chain.

For high amplitude, long duration impacts, for which plastic dissipation continues as the wave propagates, the leading wave travels without dispersion at nearly constant amplitude predicted by the upper bound. This upper bound depends solely on the material properties of the constituent particles. We use these findings to predict the wave propagation properties of chains of uniform materials, new combinations of materials, and chains of engineered particles. We support our finding with experimental tests performed in a Hopkinson bar setup equipped with a laser vibrometer.

Extensions of this work will explore high amplitude stress waves propagation in 2D and 3D elastic–plastic granular materials. Fundamental studies to understand higher dimensional systems will provide the basis to create materials with highly controllable anisotropic wave speeds, that are dispersion-free and only slightly amplitude dependent. These materials could be used to control and redirect impact energy, without relying on previous knowledge of the amplitude and frequency spectrum of the impact.

## Acknowledgment

**Appendix: Elastic–Plastic Contact Model.** The elastic–plastic contact model developed in Ref. [31] is included here for completeness. The force $F$ for a given relative compression between spheres is taken to be

$$F(\delta) = \begin{cases} (4/3)E^*\sqrt{r^*}\delta^{3/2} & \text{for} \quad 0 < \delta < \delta_y \\ \delta(\alpha + \beta \ln \delta) & \text{for} \quad \delta_y < \delta < \delta_p \\ c_1\sigma_y(2r^*\delta + c_2) & \text{for} \quad \delta > \delta_p \end{cases} \quad \text{(A1)}$$

The effective Young's Modulus is $E^* = \left(\dfrac{1-v^2}{E_1} + \dfrac{1-v^2}{E_2}\right)^{-1}$, where $E_1$, $E_2$, and $v$ are the Young's Moduli and the Poisson's Ratio of the two materials and the effective radius as $r^* = (1/r_1 + 1/r_2)^{-1}$, where $r_1$ and $r_2$ are the radii of the two

spheres. The first region ends at the onset of plasticity determined using the Von Mises criterion to be at a displacement $\delta_y$ and force $F_y$ given by

$$\delta_y = \frac{1}{4}\frac{r^*}{(E^*)^2}(1.6\sigma_y\pi)^2, \quad F_y = \frac{1}{6}\left(\frac{r^*}{E^*}\right)^2(1.6\sigma_y\pi)^3 \quad \text{(A2)}$$

For spheres of identical radius ($R$), $\sigma_y$ was modified for rate-dependent materials using a Johnson–Cook type relation

$$\sigma_y = \sigma_{y0}(1 - Cln(\dot{\varepsilon}/\dot{\varepsilon}_0)) \quad \text{(A3)}$$

where $\sigma_{y0}$ is the minimum yield stress of the two particles as measured at quasi-static strain rate $\dot{\varepsilon}_0$, and $C$ is the experimentally measured Johnson–Cook parameter. Strain rate is given by: $\dot{\varepsilon} = |v_2 - v_1|/2R$, where $v_1$ and $v_2$ are the velocities of the two particles and $R$ is their radius.

The empirical parameters were determined through FEM simulations of 6.35 mm diameter hemispheres, but can be applied to other radii with appropriate scaling (with $r^*$ in units of meters) is given by

$$\delta_p = \left[0.0043\left(\frac{E^*}{\sigma_y}\right)^{-1} + 1.47 \times 10^{-5}\right]\left(\frac{r^*}{0.00159}\right),$$

$$c_1 = -6.76\left(\frac{E^*}{\sigma_y}\right)^{-0.137} + 6.30, \quad \text{(A4)}$$

$$c_2 = \left[-3.99 \times 10^{-6}\left(\frac{E^*}{\sigma_y}\right)^{-1} + 1.01 \times 10^{-9}\right]\left(\frac{r^*}{0.00159}\right)^2$$

$\alpha$ and $\beta$ are solved for to ensure continuity between the three regions and are found to be

$$\alpha = \frac{\delta_p F_y \ln\delta_p - \delta_y F_p \ln\delta_y}{\delta_y\delta_p\left(ln\delta_p - \ln\delta_y\right)}, \quad \beta = \frac{\delta_y F_p - \delta_p F_y}{\delta_y\delta_p\left(\ln\delta_p - \ln\delta_y\right)} \quad \text{(A5)}$$

where $F_p$ is the force at which $\delta_p$ is reached: $F_p = c_1\sigma_y\left(2r^*\delta_p + c_2\right)$.

The unloading is described the formulation used by Wang et al. [30] with force given by

$$F_{un} = \frac{4}{3}E^*\sqrt{r_p}(\delta - \delta_R)^{3/2} \quad \text{(A6)}$$

where $r_p$ is the contact radius after plastic deformation, given by $r_p = \frac{4E^*}{3F_{\max}}\left(2F_{\max} + \frac{F_y}{2\pi(1.6\sigma_y)}\right)^{3/2}$ and $\delta_R$ is the residual permanent deformation, given by $\delta_R = \delta_{\max} - \left(\frac{3F_{\max}}{4E^*\sqrt{r_p}}\right)^{2/3}$. $F_{\max}$ and $\delta_{\max}$ are the force and displacement at which unloading begins.

# References

[1] Nesterenko, V., 2001, *Dynamics of Heterogeneous Materials*, Springer, New York.
[2] Job, S., Melo, F., Sokolow, A., and Sen, S., 2007, "Solitary Wave Trains in Granular Chains: Experiments, Theory, and Simulations," Granular Matter, **10**(1), pp. 13–20.
[3] Daraio, C., Nesterenko, V. F., Herbold, E. B., and Jin, S., 2006, "Tunability of Solitary Wave Properties in One-Dimensional Strongly Nonlinear Phononic Crystals," Phys. Rev. E, **73**(2), p. 026610.
[4] Doney, R. L., Agui, J. H., and Sen, S., 2009, "Energy Partitioning and Impulse Dispersion in the Decorated, Tapered, Strongly Nonlinear Granular Alignment: A System With Many Potential Applications," J. Appl. Phys., **106**(6), p. 064905.
[5] Nesterenko, V. F., Daraio, C., Herbold, E. B., and Jin, S., 2005, "Anomalous Wave Reflection at the Interface of Two Strongly Nonlinear Granular Media," Phys. Rev. Lett., **95**(15), p. 158702.
[6] Daraio, C., Nesterenko, V. F., Herbold, E. B., and Jin, S., 2006, "Energy Trapping and Shock Disintegration in a Composite Granular Medium," Phys. Rev. Lett., **96**(5), p. 058002.
[7] Fraternali, F., Porter, M. A., and Daraio, C., 2008, "Optimal Design of Composite Granular Protectors," Mech. Adv. Mater. Struct., **17**(1), pp. 1–19.
[8] Hong, J., 2005, "Universal Power-Law Decay of Impulse Energy in Granular Protectors," Phys. Rev. Lett., **94**(10), p. 108001.
[9] Ngo, D., Fraternali, F., and Daraio, C., 2012, "Highly Nonlinear Solitary Wave Propagation in Y-Shaped Granular Crystals With Variable Branch Angles," Phys. Rev. E, **85**(3), p. 036602.
[10] Leonard, A., Ponson, L., and Daraio, C., 2014, "Wave Mitigation in Ordered Networks of Granular Chains," J. Mech. Phys. Solids, **73**, pp. 103–117.
[11] Jayaprakash, K. R., Starosvetsky, Y., and Vakakis, A. F., 2011, "New Family of Solitary Waves in Granular Dimer Chains With No Precompression," Phys. Rev. E, **83**(3), p. 036606.
[12] Molinari, A., and Daraio, C., 2009, "Stationary Shocks in Periodic Highly Nonlinear Granular Chains," Phys. Rev. E, **80**(5), p. 056602.
[13] Porter, M. A., Daraio, C., Herbold, E. B., Szelengowicz, I., and Kevrekidis, P. G., 2008, "Highly Nonlinear Solitary Waves in Periodic Dimer Granular Chains," Phys. Rev. E, **77**(1), p. 015601.
[14] Bragança, E. A., Rosas, A., and Lindenberg, K., 2013, "Binary Collision Approximation for Multi-Decorated Granular Chains," Physica A, **392**(24), pp. 6198–6205.
[15] Sen, S., Hong, J., Bang, J., Avalos, E., and Doney, R., 2008, "Solitary Waves in the Granular Chain," Phys. Reports, **462**(2), pp. 21–66.
[16] Boechler, N., Yang, J., Theocharis, G., Kevrekidis, P. G., and Daraio, C., 2011, "Tunable Vibrational Band Gaps in One-Dimensional Diatomic Granular Crystals With Three-Particle Unit Cells," J. App. Phys., **109**(7), p. 074906.
[17] Hoogeboom, C., Man, Y., Boechler, N., Theocharis, G., Kevrekidis, P. G., Kevrekidis, I. G., and Daraio, C., 2013, "Hysteresis Loops and Multi-Stability: From Periodic Orbits to Chaotic Dynamics (and Back) in Diatomic Granular Crystals," Europhys. Lett., **101**(4), p. 44003.
[18] Herbold, E. B., Kim, J., Nesterenko, V. F., Wang, S., and Daraio, C., 2009, "Pulse Propagation in a Linear and Nonlinear Diatomic Periodic Chain: Effects of Acoustic Frequency Band-Gap," Acta Mech., **205**(1–4), pp. 85–103.
[19] Breindel, A., Sun, D., and Sen, S., 2011, "Impulse Absorption Using Small, Hard Panels of Embedded Cylinders With Granular Alignments," App. Phys. Lett., **99**(6), p. 063510.
[20] Tournat, V., Gusev, V. E., and Castagnede, B., 2004, "Self-Demodulation of Elastic Waves in a One-Dimensional Granular Chain," Phys. Rev. E, **70**(5), p. 056603.
[21] Ganesh, R., and Gonella, S., 2014, "Invariants of Nonlinearity in the Phononic Characteristics of Granular Chains," Phys. Rev. E, **90**(2), p. 023205.
[22] Cabaret, J., Tournat, V., and Bequin, P., 2012, "Amplitude-Dependent Phononic Processes in a Diatomic Granular Chain in the Weakly Nonlinear Regime," Phys. Rev. E, **86**(4), p. 041305.
[23] Coste, C., and Gilles, B., 1998, "On the Validity of Hertz Contact Law for Granular Material Acoustics," Eur. Phys. J. B, **7**(1), pp. 155–168.
[24] Pal, R. K., Awasthi, A. P., and Geubelle, P. H., 2013, "Wave Propagation in Elasto-Plastic Granular Systems," Granular Matter, **15**(6), pp. 747–758.
[25] Pal, R. K., Awasthi, A. P., and Geubelle, P. H., 2014, "Characterization of Wave Propagation in Elastic and Elastoplastic Granular Chains," Phys. Rev. E, **89**(1), p. 012204.
[26] Wang, E., Manjunath, M., Awasthi, A. P., Pal, R. K., Geubelle, P. H., and Lambros, J., 2014, "High-Amplitude Elastic Solitary Wave Propagation in 1-D Granular Chains With Preconditioned Beads: Experiments and Theoretical Analysis," J. Mech. Phys. Solids, **72**, pp. 161–173.
[27] Shoaib, M., and Kari, L., 2011, "Discrete Element Simulations of Elastoplastic Shock Wave Propagation in Spherical Particles," Adv. Acoust. Vib., **2011**, pp. 1–9.
[28] Thornton, C., 1995, "Coefficient of Restitution for Collinear Collisions of Elastic-Perfectly Plastic Spheres," ASME J. Appl. Mech., **62**(2), pp. 383–386.
[29] Vu-Quoc, L., Zhang, X., and Lesburg, L., 1999, "A Normal Force–Displacement Model for Contacting Spheres Accounting for Plastic Deformation: Force-Driven Formulation," ASME J. Appl. Mech., **67**(2), pp. 363–371.
[30] Wang, E., On, T., and Lambros, J., 2013, "An Experimental Study of the Dynamic Elasto-Plastic Contact Behavior of Dimer Metallic Granules," Exp. Mech., **53**(5), pp. 883–892.
[31] Burgoyne, H. A., and Daraio, C., 2014, "Strain-Rate-Dependent Model for the Dynamic Compression of Elastoplastic Spheres," Phys. Rev. E, **89**(3), p. 032203.
[32] On, T., LaVigne, P. A., and Lambros, J., 2014, "Development of Plastic Nonlinear Waves in One-Dimensional Ductile Granular Chains Under Impact Loading," Mech. Mater., **68**, pp. 29–37.
[33] Pal, R. K., Morton, J., Wang, E., Lambros, J., and Geubelle, P. H., 2015, "Impact Response of Elasto-Plastic Granular Chains Containing an Intruder Particle," ASME J. Appl. Mech., **82**(1), p. 011002.
[34] On, T., Wang, E., and Lambros, J., "Plastic Waves in One-Dimensional Heterogeneous Granular Chains Under Impact Loading: Single Intruders and Dimer Chains," Int. J. Solids Struct., **61**, pp. 81–90.
[35] Wang, E., Geubelle, P., and Lambros, J., 2013, "An Experimental Study of the Dynamic Elasto-Plastic Contact Behavior of Metallic Granules," ASME J. Appl. Mech., **80**(2), p. 021009.
[36] Gray, G. T., 2000, "Classic Split-Hopkinson Pressure Bar Testing," *ASM Handbook: Mechanical Testing and Evaluation*, Vol. 8, ASM International, Novelty, OH.
[37] Stratasys, 2014, "PolyJet Materials Data Sheet," Stratasys, Eden Prarie, MN, http://www.stratasys.com/~/media/main/secure/material%20specs%20ms/polyjet-material-specs/polyjet_materials_data_sheet.pdf
[38] Daraio, C., Nesterenko, V. F., Herbold, E. B., and Jin, S., 2005, "Strongly Nonlinear Waves in a Chain of Teflon Beads," Phys. Rev. E, **72**(1), p. 016603.
[39] Ashcroft, N. W., and Mermin, N. D., 1976, *Solid State Physics*, Saunders College Publishing, Orlando, FL.
[40] Hascoet, E., Herrmann, H. J., and Loreto, V., 1999, "Shock Propagation in a Granular Chain," Phys. Rev. E, **59**(3), pp. 3202–3206.
[41] Tasi, J., 1980, "Evolution of Shocks in a One Dimensional Lattice," J. Appl. Phys., **51**(11), pp. 5804–5815.
[42] Zhuang, S., Ravichandran, G., and Grady, D. E., 2003, "An Experimental Investigation of Shock Wave Propagation in Periodically Layered Composites," J. Mech. Phys. Solids, **52**(2), pp. 245–265.